Investigation of Drag Modulated Supersonic Inflatable Aerodynamic Decelerators for Use on Sounding Rocket Payloads

AE 8900 MS Special Problems Report
Space Systems Design Lab (SSDL)
Guggenheim School of Aerospace Engineering
Georgia Institute of Technology
Atlanta, GA

Author:
Matthew J. Miller

Advisor:
Prof. Robert D. Braun

December 13, 2013

Investigation of Drag Modulated Supersonic Inflatable Aerodynamic Decelerators for Use on Sounding Rocket Payloads

Matthew J. Miller,[1] Bradley A. Steinfeldt,[2] Robert D. Braun[3]
Georgia Institute of Technology, Atlanta, GA, 30332

This paper presents an assessment of use of a supersonic inflatable aerodynamic decelerator for drag modulation of a sounding rocket payload bus structure as part of a high-altitude sample return mission. The scientific goal of this mission is to capture mesospheric dust and particulate matter located 45 km to 85 km in altitude. This mission is also to demonstrate technology that is capable of precise landings by combining a decelerator system comprised of inflatable aerodynamic decelerator to reach within 10 km with a guided parafoil system. Three decelerator configurations, the tension cone, attached isotensoid, and the trailing isotensoid, were examined on the metrics of decelerator mass, aerodynamic performance, and vehicle integration. The attached isotensoid was found to be the most mass efficient option, while the trailing isotensoid was determined to be preferable from an overall system level perspective. The decelerators' precision landing capability through the use of drag modulation was also evaluated. Downrange error was reduced by 21% by drag modulation as compared to an 8.5 m supersonic disk-gap-band parachute. When coupled with a guided parafoil, drag modulation provides a 95% confidence level in landing within the 10 km parafoil capability region, and a 76% confidence level of landing within 5 km of the target.

Nomenclature

A	= area, m^2	q_{deploy}	= deployment dynamic pressure, Pa
C_D	= coefficient of drag	ρ	= atmospheric density, kg/m^3
C_DA	= drag area, m^2	S_0	= reference area, m^2
C_X	= drag coefficient correction factor	T_0	= stagnation temperature, K
d_f	= areal density, kg/m^2	t	= time, s
ε_t	= ratio of minor torus diameter to overall diameter	t_{SI}	= inflation start time, s
M	= Mach number	t_{FI}	= time at full inflation, s
n	= inflation power constant	v	= velocity, m/s

I. Introduction

The mesosphere which ranges in altitude from 45 km to 85 km has been a region of scientific interest for decades. Scientific estimates predict between 10 and 100 t of meteoric material, micron to nanometer in size, enters the Earth's atmosphere per day [1] [2]. These particles have been linked to polar summer mesospheric phenomena such as noctiluent clouds and polar mesosphere summer echoes [3] [4]. Also known as meteoric smoke, mesospheric dust has been implicated in other atmospheric processes such as the production of nitric acid [5], the removal of HNO_3 from the lower stratosphere [6], which alters ozone chemistry, and the condensation of sulphate aerosols in the stratosphere [7]. Various origins of the dust present in the mesosphere exist, including 2-5% of the matter which is estimated to have originated from interstellar space [8] [9]. The composition and conditions of particle genesis of meteor smoke is highly sought after to further refine the scientific theories and models of the aforementioned atmospheric processes [10].

[1] Graduate Research Assistant, Guggenheim School of Aerospace Engineering, mmiller@gatech.edu, AIAA Student Member
[2] Research Engineer II, Guggenheim School of Aerospace Engineering, bsteinfeldt@gatech.edu, AIAA Member
[3] David and Andrew Lewis Associate Professor of Space Technology, Guggenheim School of Aerospace Engineering, robert.braun@aerospace.gatech.edu, AIAA Fellow

Numerous attempts to capture mesospheric dust for laboratory analysis have had moderate success. Figure 1 shows historical sample collection campaigns, which began in the early 1960's. These early missions consisted of payload devices such as the Venus Flytrap [11], Luster device [12] [13] [14] [15] [16], and the ALARR device [13].

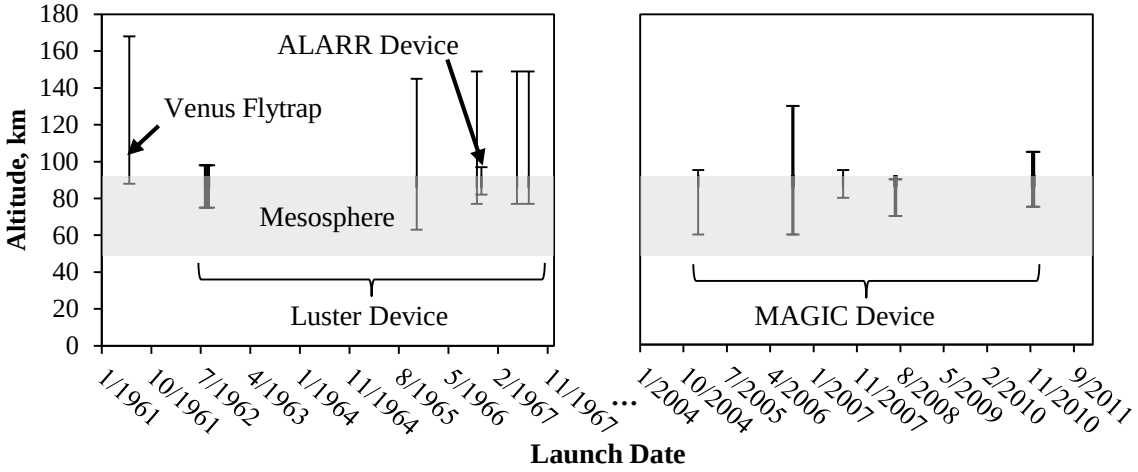

Figure 1. Altitude range for previous sample collection missions conducted on sounding rockets.

Each device, launched on a sounding rocket, was comprised of contaminant-free flat plate sampling surfaces which were exposed perpendicular to the freestream between the altitudes shown in Figure 1. These devices were limited to capturing micron-sized or larger particles because submicron and nanometer scale particles tend to follow the flow around the payload thus not reaching the capturing surface [17]. In a continuing effort to examine the middle atmosphere, *in-situ* particle measuring payloads were developed in the late 1980's and 1990's such as DROPPS, TURBO, MIDAS, Mini-MIDAS, and Mini-Dusty. More detailed information regarding *in-situ* measure payloads and campaigns can be found in Refs. [18], [19], [20], [21].

Within the last decade, there has been a renewed effort to capture mesospheric dust for laboratory analysis. The MAGIC (Mesospheric Aerosol – Genesis, Interaction and Composition) device was developed and flew its maiden flight early in 2005. This device specifically targets the nanometer scale meteoric particles that reside in the mesosphere. More detailed information regarding this payload device and its performance can be found in Refs. [22] [23] [24]. In line with these recent efforts, this systems study contributes to the effort of capturing upper atmospheric particle, with an emphasis on precision recovery using an inflatable aerodynamic decelerator (IAD).

First proposed in the 1960's, IADs are devices capable of increasing a vehicle's drag area. Compared to conventional parachute technology, IADs are capable of being deployed at higher dynamic pressures and Mach numbers enabling additional deceleration [25]. This study focuses on IADs which operate in the supersonic Mach number regime and are known as supersonic IADs. Numerous flight tests were conducted until the mid 1970's which examined the aerodynamic drag performance and stability of IADs [26] [27]. At present, NASA is investigating this technology through the LDSD program [28]. A typical use for an IAD is to increase the landed mass of an entry vehicle on a planetary body. However, the focus of this study is centered on the IAD's capability to perform as a precision-enhancing device for payload pinpoint landing.

The study is broken into two phases: 1) supersonic decelerator evaluation in terms of aerodynamics, mass, and vehicle integration, and 2) a suborbital sounding rocket trajectory evaluation with drag modulation. Phase 1 includes the examination of three inflatable aerodynamic decelerators: a tension cone, attached isotensoid, and trailing isotensoid. Phase 2 integrates the IADs into a trajectory simulation which was optimized for maximum science return and increased landed precision.

II. Mission Architecture

A. Mission and Objective Definition

This study was developed in an effort to provide a cost-effective and reliable method of acquiring samples of matter, including particles and dust, from Earth's mesosphere and returning them to Earth's surface precisely. The primary objectives include obtaining a scientifically significant sample of matter (particles and dust) from Earth's mesosphere (45 – 85 km) and returning the collected matter from Earth's mesosphere safely to the surface of Earth

for recovery and analysis. The purpose of this study is to examine the effect of implementing a supersonic IAD to achieve the aforementioned mission objectives and examine the capability to perform precision recovery.

B. Design Space

In order to evaluate the precision capability of implementing supersonic IADs on sounding rockets, three candidate reference architectures were formulated as shown in previous work [29]. Figure 2 shows the three architectures that were examined. Architecture #1 represents a mesospheric sample collection platform which utilizes stock sounding rocket decelerator hardware (an 8.5 m supersonic disk-gap-band (DGB) parachute). Architecture #2 represents a mesospheric sample collection platform which utilizes a supersonic IAD. This device is capable of deploying in flow environments up to Mach 4 and 25 kPa dynamic pressure [25]. Less severe deployment conditions, Mach 3 and 2 kPa, were predicted for a 45km altitude deployment. Finally, Architecture #3 represents a mesospheric sample collection platform which utilizes a drag modulated supersonic IAD and a precision guided parafoil to demonstrate a more precise return of a suborbital sample retrieval system. The drag modulated downrange capability is enhanced by the maneuvering of a guided parafoil which is nominally deployed at 6 km altitude. For a more detailed description of these architectures, see Ref. [29].

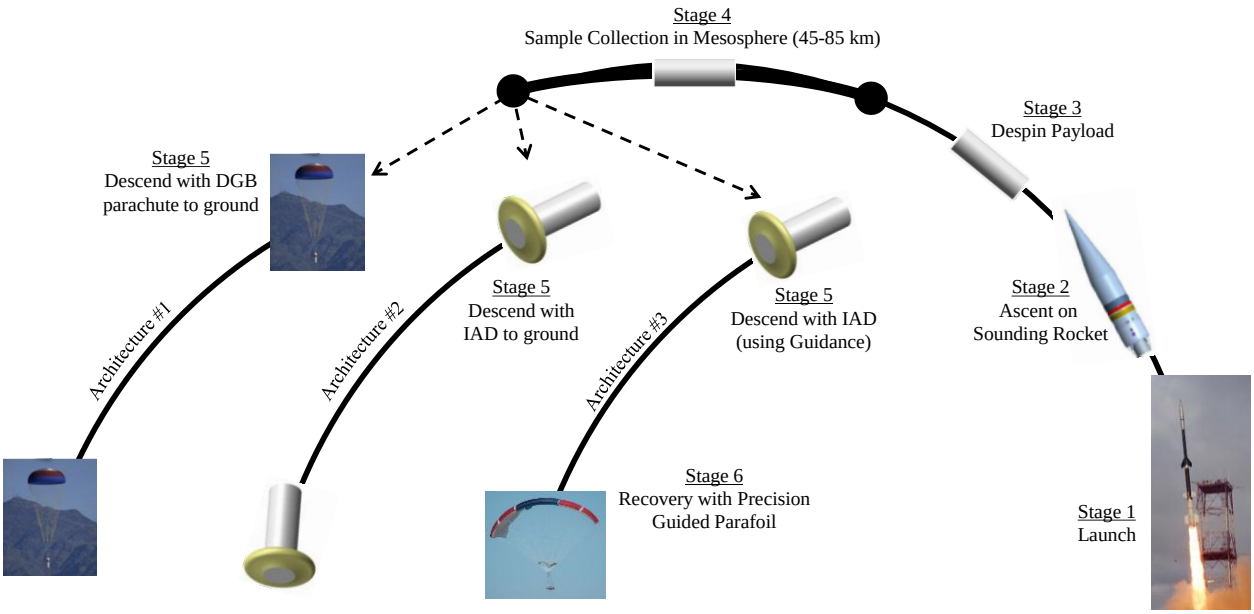

Figure 2. Baseline mission architecture trajectory profiles.

C. Sounding Rocket Configuration

The NASA sounding rocket program conducts a variety of sounding rocket launches for a multitude of different mission profiles each year. After evaluation of the various sounding rockets, the Improved-Orion sounding rocket was selected for this study. The Improved-Orion provides the launch capability necessary to reach the mesosphere while being able to accommodate a variety of payload diameters, 4.5 to 17 inches, with its bulbous fairing option, as shown in Figure 3 [30].

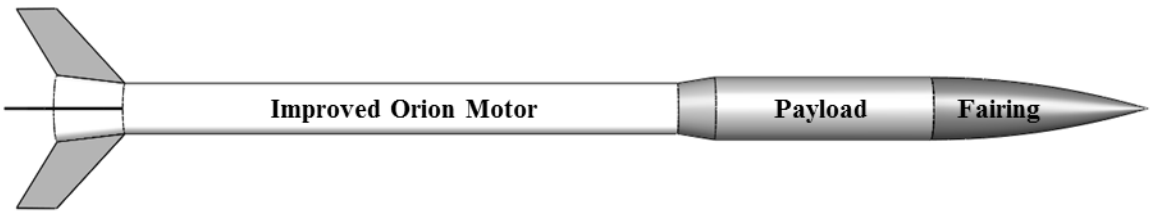

Figure 3. Improved Orion sounding rocket with bulbous payload fairing.

1. Payload Bus & Sample Collection Device

Typical payload configurations for the launch vehicles under consideration utilize a cylinder with a diameter of 0.356 m and a length of 1.22 m as shown in Figure 4. The sample collection mechanism was assumed to be a container fitted with Aerogel pucks. Aerogel was proven as a viable medium for capturing high velocity particles in outer space on the Stardust mission [31] and could be implemented for sounding rocket particle capturing. The detailed design of the sample collection device is outside the scope of this study; however, it is assumed that the Aerogel would be exposed to the freestream during the sample collection phase without altering the vehicle aerodynamics. After sample collection, the containment device would seal the Aerogel pucks, preventing the samples from being contaminated during recovery. The trajectory analysis includes an analysis of the quantity of samples that can be collected using the frontal area of the vehicle bus based on dust particle profiles published by Hunten, et al. [32].

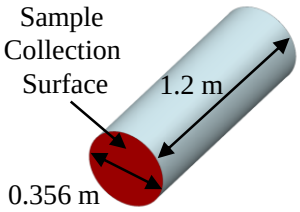

Figure 4. Representative cylindrical bus structure.

D. Decelerator Configurations

1. Attached Tension Cone

The tension cone consists of two primary fabric components: a flexible shell that resists shape deformation by remaining under tension and an inflated torus. The curvature is analytically derived based on a pressure distribution and assumed constant ratio of circumferential to meridional stress. The shell of the tension cone is attached to the forebody at the front of the vehicle and to an inflated torus. An onboard inflation system is required to inflate the torus and to maintain the internal pressure of the torus. The baseline tension cone for this study had an overall diameter of 0.9 m with a torus diameter of 0.1125 m as shown in Figure 5. A detailed description of tension cone IADs can be found in [33].

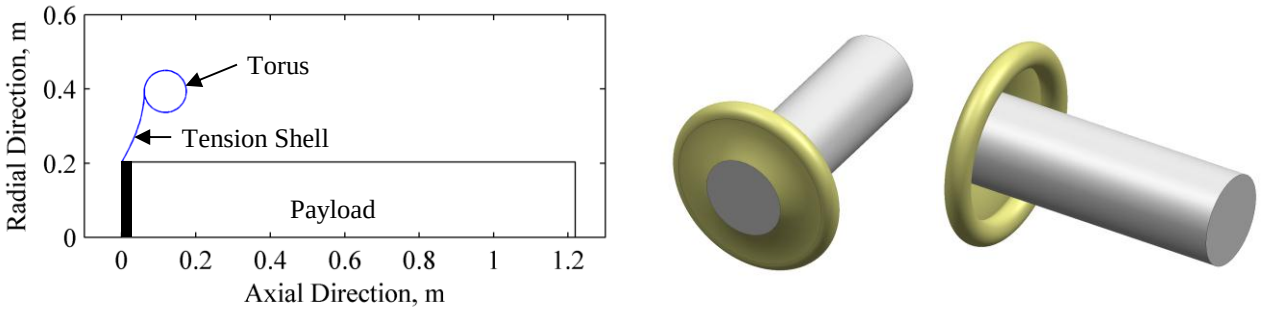

(a) **(b)** **(c)**

Figure 5. Tension cone (a) dimensions, (b) frontward isometric, and (c) rearward isometric integrated with payload bus structure.

2. Attached Isotensoid

The isotensoid configuration is examined as an attached and trailing configuration. The decelerator itself is largely the same for each configuration, except for how the decelerator is integrated with the bus structure. The isotensoid shape enables constant tension throughout the length of the meridians and a uniform biaxial stress across the gore fabric. Ram air inlets, not shown in Figure 6, maintain internal pressure of the device, thus no onboard inflation system is required to maintain the inflated shape. However, a pre-inflation system is typically needed to subject the ram air inlets to the freestream for inflation to start. The attached isotensoid shape used in this study was derived from the work conducted by Barton in Ref. [34] and had an overall diameter of 0.99 meters which includes the burble fence. A detailed description of the isotensoid can be found in [34] [35].

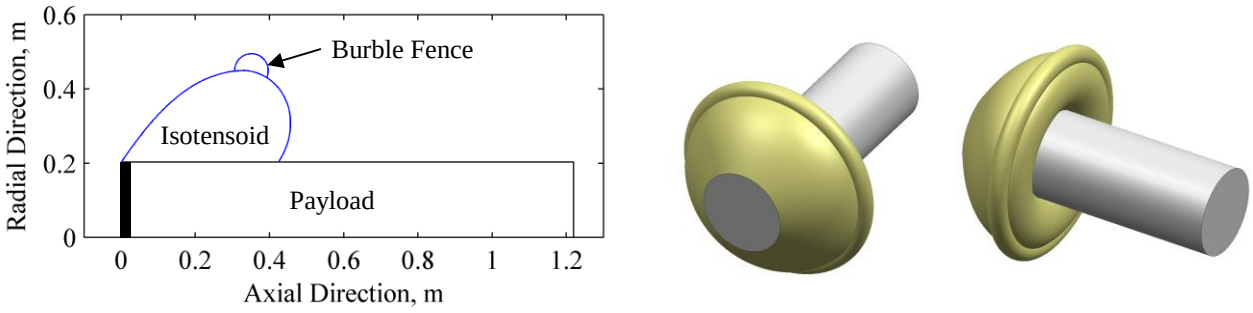

(a) **(b)** **(c)**

Figure 6. Attached isotensoid (a) dimensions, (b) frontward isometric, and (c) rearward isometric integrated with payload bus structure.

3. Trailing Isotensoid

The trailing isotensoid is deployed by an ejection event and trails behind the vehicle's bus. The decelerator inflates in a similar manner as the attached isotensoid, except the device is located at some predefined trailing length behind the bus. The representative trailing isotensoid for this study, as shown in Figure 7, was taken from Ref. [36].

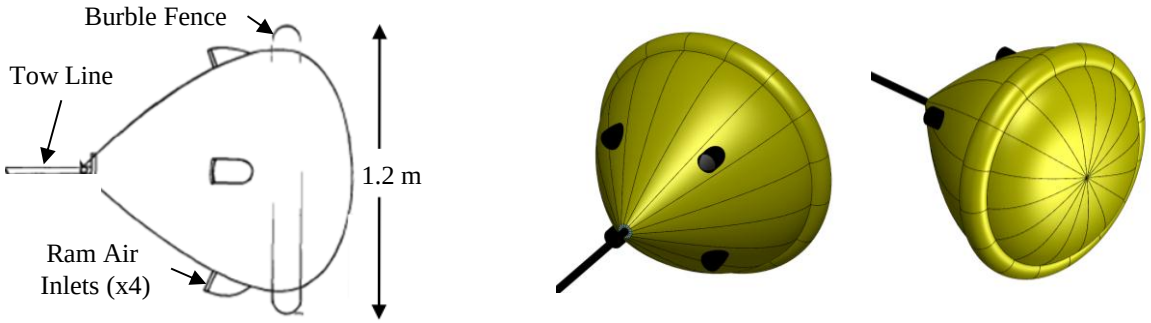

(a) [36] **(b)** **(c)**

Figure 7. Trailing isotensoid (a) dimensions, (b) frontward isometric, and (c) rearward isometric integrated with payload bus structure.

4. Disk-Gap-Band Parachute

For comparison, an 8.5 m supersonic DGB parachute was examined in Architecture #1. This decelerator provides a stock sounding rocket decelerator option for payload recovery [30]. The DGB decelerator option offers a baseline precision recovery performance to which more elaborate recovery configurations can be compared.

5. Precision Guided Parafoil

In order to achieve precision landing capability [37] [38] [39], a precision guided parafoil was considered as a terminal decent stage decelerator for this study. The dynamics of this device was not explicitly model. Instead, previous work was leveraged to estimate the parafoil capability. For this study, the 40 ft^2 Mosquito Parafoil with an estimated lift-to-drag ratio of 3 and a circular capability region of a 10 km radius was assumed [40].

III. Modeling

A. Aerodynamics

Two types of aerodynamics analyses were implemented to characterize the aerodynamic performance of the tension cone and attached isotensoid aerodynamic decelerators—a hypersonic panel method with engineering correlations to the supersonic regime, CBAERO [41], and a computational fluid dynamics (CFD) package, FUN3D. Trailing isotensoid aerodynamic performance was obtained from heritage wind tunnel and in-flight experimentation. Calculation of the interactions of blunt body wakes on trailing decelerators is outside of the scope of this study. Therefore, the heritage sources were leveraged for the trailing decelerator. All aerodynamic performance values were generated at zero angle-of-attack relative to the free stream.

1. Computational Fluid Dynamics Method

The CFD simulation was performed in FUN3D. FUN3D is a fully unstructured, 3-dimesional fluid solver with both Euler and Reynolds average Navier Stokes equation capabilities [42] [43]. For this study, inviscid, calorically perfect, compressible equations were assumed with local time stepping. Grids were generated using Gridgen [44] and consist of between 0.8 and 0.9 million grid points. All CFD solutions were generated using the input variable values shown in Table I.

Table I. FUN3D parameters.

Variable	Value	Units
M	4.0	-
ρ	0.0577	kg/m^3
T_0	219	K
V	1,181	m/s

2. Sounding Rocket, Payload Bus, and Decelerator Aerodynamics

This study incorporated Mach-dependent aerodynamics for the sounding rocket and cylindrical bus structure. The drag coefficient values as a function of Mach number for the bulbous sounding rocket payload fairing was estimated to be similar to that of the 5.56mm BRL-1 ballistic projectile [45] and reference literature was used for the cylindrical bus structure [46]. Since the vehicle is symmetric and assumed to be flying a zero degrees angle-of-attack, the lift coefficients for the sounding rocket and decelerator are assumed to be zero. The Mach-dependent drag coefficients used in this study for the sounding rocket, bus, and various decelerators are seen in Figure 8.

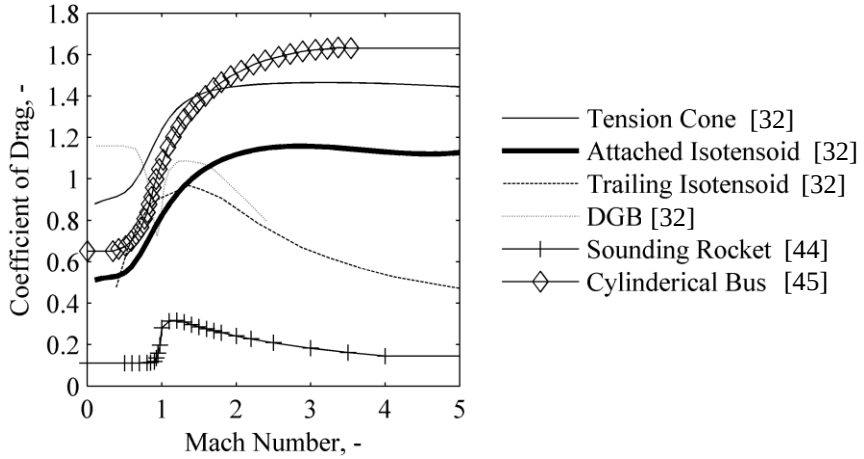

Figure 8. Mach dependent aerodynamics for the sounding rocket and cylindrical bus and decelerators.

A stock high altitude sounding rocket DGB deployed at 73 km altitude with 25 seconds of inflation time was modeled [47]. The DGB parachute has extensive flight demonstration and performance capability [47] [48]. Parachute inflation loads were estimated using the opening loads equation shown in Equation 1 where q is the dynamic pressure of the freestream, C_{D0}, is the drag coefficient of the DGB parachute, S_0 is the reference drag area of the DGB parachute, C_X is a drag coefficient correction factor, 1.45, t, is the time step of the solver, t_{SI} is the time at start of inflation, t_{FI} is the time at full inflation, and n is a power constant (assumed to be 2 for this analysis) [49].

$$F_p = qC_{D0}S_0C_X\left(\frac{t - t_{SI}}{t_{FI} - t_{SI}}\right)^n \quad (1)$$

The 8.5 m DGB upper mass limit of 24 kg as well as the cylindrical bus configuration was implemented in this study as the baseline vehicle configuration [30]. A 0.9 m diameter IAD was also implemented in this analysis as an alternative supersonic decelerator option. The guided parachute deployment constraints were accounted for even though this phase was not explicitly simulated [50] [51]. Deployment constraints are summarized in Table II for all deployables.

Table II. Deployment constraints for deployable devices.

Deployable Type	Deployment Conditions	
	Mach Number	*Dynamic Pressure (kPa)*
DGB	1.0 - 2.5	4x10^{-5} - 0.9
IAD	1.0 - 4.0	1x10^{-3} - 25
Guided Parafoil	0.01 - 0.15	4x10^{-5} - 1.2

B. Mass Estimation

To account for the mass addition of each decelerator system, mass estimates were obtained for all three aerodynamic decelerators based on parametric sizing techniques and historical regressions.

1. *Attached Tension Cone*

The mass for the tension cone was determined using the dimensionless parameter technique developed by Samareh [52]. The total tension cone system's mass was calculated by the summation of eight different dimensionless elements: the inflation gas, the inflation systems mass, the toroid fiber mass, the toroid adhesive mass, the toroid gas barrier mass, the toroid axial straps mass, the radial straps mass, and the gore mass.

The tension cone input configuration for this study is summarized in Table III. All other input parameters used in Samareh's mass sizing technique were assumed to be the same as referenced in Ref. [52]. A 30% mass margin was added to the final masses to account for any miscellaneous mass and uncertainty not accounted for in this analysis.

Table III. Tension cone input parameters.

Input Parameter	Value
Dynamic Pressure (Pa)	2000
Number of Toroid	1
Area Ratio	6.39
Radius Ratio	7
Diameter of Torus Circle (m)	0.1125
Diameter of Torus (m)	0.7875
ε_t (D_t/D_0)	0.1429
Vehicle Bus Diameter (m)	0.356
Tension Cone Drag Coefficient	1.5
Number of Radial Straps	16

2. *Trailing Isotensoid*

The trailing isotensoid mass was calculated using a relationship accounting for the structural and aerodynamic parameters which govern the decelerator efficiency [53]. Equation 2 shows this relation where the first term accounts for the mass of meridian tapes and rise and suspension lines and the second term accounts for the canopy mass.

$$m_{Iso} = bq_{deploy}(C_D A)^{3/2} + cd_f(C_D A) \tag{2}$$

The aerodynamic drag area ($C_D A$) is of the trailing isotensoid only. The constants *b* and *c*, which were derived from pressure vessel theory, are specified by Anderson to be $6.9\text{x}10^{-5}$ kg/N-m and 7.41, respectively [53]. From the baseline trajectory, the dynamic pressure at deployment is 2 kPa and d_f is the areal density of the canopy fabric (kg/m^2). A 50% mass margin is added to final masses to account for any miscellaneous mass and uncertainty not accounted for in this analysis.

The deployment mechanism for the trailing isotensoid requires a mortar similar to that of a typical parachute system [33]. The mortar mass required to eject a given trailing isotensoid was estimated from a linear regression of historical data for subsonic parachutes of similar masses, shown in Figure 9.

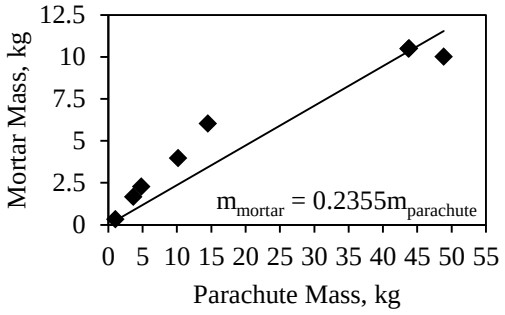

Figure 9. Mortar mass vs. parachute mass regression [32].

3. *Attached Isotensoid*

The attached isotensoid mass was calculated using the relation as the trailing isotensoid described in Eqn. (1). However, the constants *b* and *c* were altered to $1.1\text{x}10^{-5}$ kg/N-m and 4.02, respectively, to account for the changed isotensoid configuration as suggested in Ref. [53]. As with the trailing isotensoid, a 50% mass margin was also included in the attached isotensoid mass estimate to account for uncertainty associated with this empirical mass estimation method.

4. *Decelerator Material Properties*

All decelerator masses were evaluated using a variety of materials shown in Table IV, where $\bar{\sigma}$ is a non-dimensional yield stress as described in Ref. [52].

Table IV. Material properties for decelerator systems.

Material	Density (kg/m^3)	Areal Density (kg/m^2)	Tensile Strength (GPa)	$\bar{\sigma}$ (-)	Reference
Vectran	1,400	0.0916	1.10	80,093	[54] [55]
(Coated) Vectran	1,500	0.1457	3.20	217,465	[54] [55]
Kevlar 29	1,440	0.2080	2.92	206,705	[56] [57]
Kevlar 49	1,440	0.1810	3.00	212,368	[56] [57]
(Coated) Kevlar	1,500*	0.3750	3.00	203,874	[56] [57]
Upilex-25S	1,470	0.3778**	0.52	36,059	[58]
Nomex	1,380	0.4001	0.61	45,059	[59]
Nextel (610)	3,900	0.2780	3.20	83,640	[60] [33]

*Density estimated based on coated Vectran

**Upilex minimum gage areal density estimated based on 50 micrometer fabric thickness and scaled by same factor as Nomex

The materials used in this analysis encompass heritage materials such as Nomex and Nextel and more modern materials such as Vectran and Kevlar to capture the advancements that have been made in the material sciences field. Coated materials which reduce fabric porosity are also included in this study **[33]**. Areal density values are assumed to be minimum gage values with the exception of Upilex-25S and Nomex. The minimum gage areal density of Nomex is 0.078 kg/m^2; however, flight test articles from Ref. **[61]** deployed trailing decelerators at high dynamics pressures (11-17 kPa) made of Nomex with an areal density equal to 0.4 kg/m^2. The minimum gage areal density of Nomex was linearly scaled to match the test article areal density and the same scaling value was applied to Upilex-25S, since both materials share similar material properties.

C. Trajectory

A three degree-of-freedom simulation was used to propagate the trajectory. A fixed-step, 4^{th}-order Runge-Kutta algorithm with an adaptive-step integration scheme was used. The initial state corresponds to a representative state on the launch pad at White Sands Missile Range.

D. Drag Modulation

Drag modulation is a mechanism that employs a discrete event which alters the drag area of a vehicle. In this study, this discrete event is the deployment of an IAD to control vehicle downrange and deployment conditions for the parafoil deployment. For a more detailed discussion on drag modulation, refer to Refs. [62], [63]. Figure 10 shows the notional drag modulation trajectory profile incorporated into this study. Both a fixed deployment altitude trigger and a predictor-corrector trigger was implemented in this study for range control evaluation.

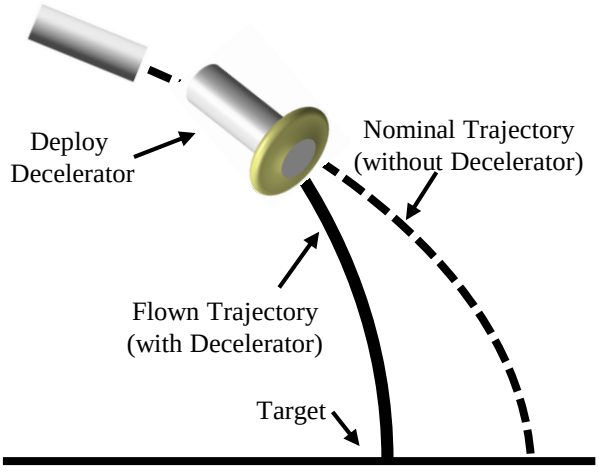

Figure 10. Drag modulated trajectory profile.

IV. Analyses

A. Dispersion Analysis

1. Monte Carlo Parameters

To investigate the overall performance improvement of drag modulation implementation, three Monte Carlo analyses of 1000 runs were conducted for various decelerator configurations. Table V shows the parameters which were varied along with their nominal value, distribution type, and deviation value. Earth-GRAM 2007 was used to generate all atmospheric information, including standard deviations as a function of altitude [64]. This study also estimated that the atmospheric dispersions generated from Earth-GRAM could be reduced to 10% of their original

dispersions as weather balloons can provide detailed day-of-launch atmospheric data [65]. Figure 11 below shows the reduced atmospheric density, Eastward and Northward wind variation as a function of altitude for the nominal launch site at White Sands.

Table V. Vehicle and state parameters [66]**.**

Parameter	Nominal Value	Distribution Type	Deviation (3-sigma or min/max)
Launch Elevation Angle, Deg	81.0	Uniform	+/- 0.1
Launch Azimuth Angle, Deg	355.0	Uniform	+/- 0.1
Payload Mass, kg	24.0	Uniform	+/- 0.5
Mass-drop Time, s	10.0	Uniform	+/- 1.0
Thrust Multiplier (Booster)	1.0	Gaussian	0.03
Thrust Multiplier (Sustainer)	1.0	Gaussian	0.03
Drag Coefficient Multiplier (Sounding Rocket)	1.0	Gaussian	0.1
Drag Coefficient Multiplier (Payload Bus)	1.0	Gaussian	0.1
Drag Coefficient Multiplier (Decelerator)	1.0	Gaussian	0.1

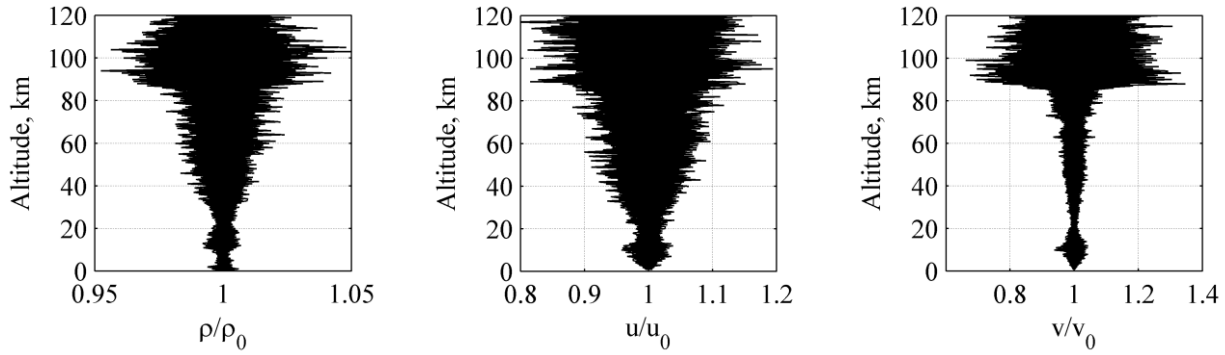

Figure 11. Atmosphere variation as a function of altitude for (a) density, (b) East winds, and (c) North winds.

B. Decelerator Evaluation

1. Aerodynamics

In addition to the nominal attachment point, the effect of attachment point locations on decelerator drag performance was also investigated. Figure 12 shows four alternative forward attachment point locations. The alternative attachment points were incremented by 5% of the length of the vehicle bus resulting in a maximum attachment point offset distance of 0.244 m from the front of the vehicle bus. These alternative attachment points were to account for the accommodation of more complicated sample collection devices.

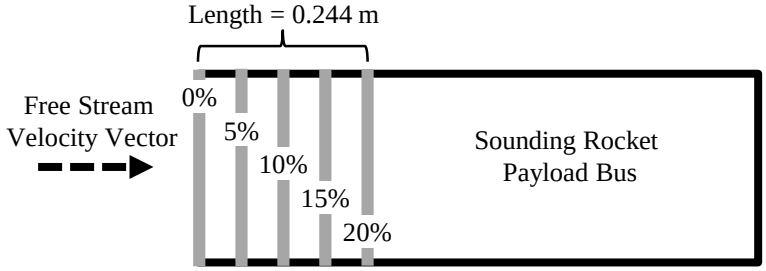

Figure 12. Decelerator front attachment point locations along the length of the vehicle bus.

2. Vehicle Integration

To evaluate each mechanism in a qualitative manner, an analytical hierarchy process (AHP) was used [67] [68]. AHP is a multi-attribute decision-making technique that uses pairwise comparisons. Prioritization of objectives is

obtained from populating a matrix of pairwise comparisons. A vector of weights indicating the relative importance of each objective is then obtained. For this study, each mechanism served as an objective and were compared to each other using an objective scoring system which ranged from extremely prefer to neutral. The storage volume for each decelerator was also examined for each decelerator assuming a nominal parachute nonpressuized packaging density of 320 kg/m^3 for a range of decelerator drag areas [49].

V. Decelerator Results and Discussion

A. Aerodynamics Results

Historical testing programs have examined the drag performance of the three decelerators under investigation for this study, see Figure 8. For this analysis, CBAERO results consistently over predicted the drag coefficient of the attached isotensoid and tension cone by approximately 13%. This consistent over prediction is attributed to CBAERO's inability to account for the drag coefficient of the front face of the cylinder. The pressure distribution on the cylinder's front face is greatly influenced by the bow shock which is not taken into account in the CBAERO panel method. The inviscid CFD solutions for both decelerators were in good agreement with historical drag coefficient values.

The aerodynamic performance of the trailing decelerator is difficult to predict due to the unsteady nature of the wake flowfield region behind the forebody bus structure. However, experimental testing showed trailing decelerators exhibit stabilizing characteristics for a variety of Mach number regimes and decelerator-to-payload size ratios [27]. Therefore, the drag coefficient trends shown in Figure 8 were directly used for the trailing isotensoid.

Aerodynamic performance of the tension cone and attached isotensoid were analyzed for a variety of attachment points, since the sample collection mechanism is not clearly defined at this stage in the design process. As the decelerator moves farther rearward, drag performance diminishes substantially as shown in Figure 14. The decelerator becomes shadowed by the oblique shock which forms from the corner of the bus forebody, thus reducing the decelerator's overall drag coefficient. The CFD Mach contour solutions to the 0% offset and 20% offset solutions for the baseline tension cone are shown in Figure 15. The bow shock changes for the varied attachment points, which results in altered pressure distributions on the surface of the decelerator. This altered pressure distribution leads to reduced drag performance for the offset attachment points. The altered bow shock also alters the pressure distribution on the bus forebody. The results from this analysis indicate that a 0% offset maximizes. Increasing the attachment offset could be accommodated by increasing the diameter of the decelerator at the cost of increasing the overall mass of the decelerator subsystem.

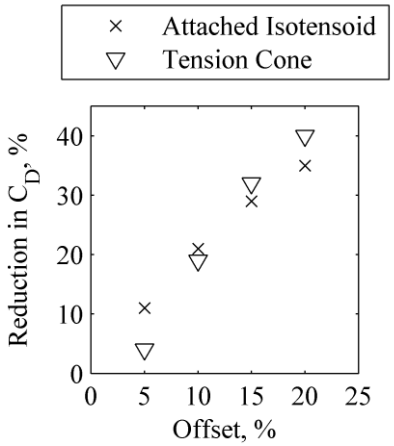

Figure 13. Drag coefficient reduction as a function of attachment offset.

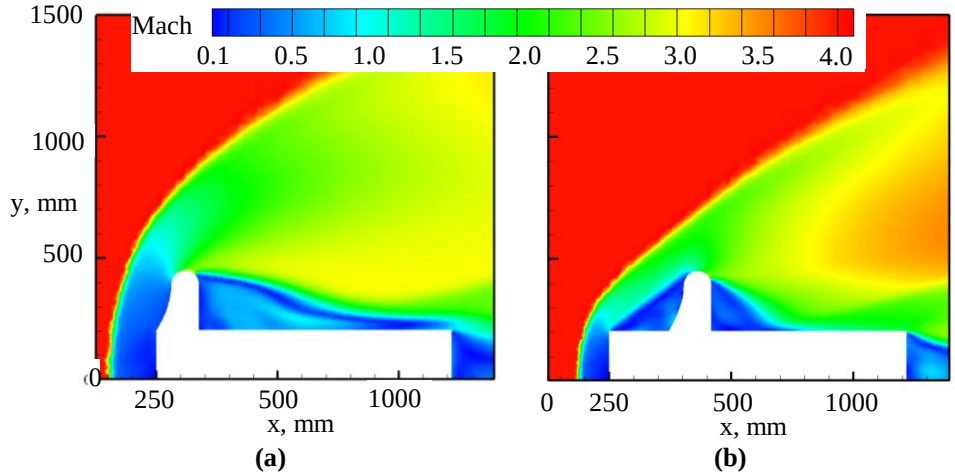

Figure 15. Mach contour plots of (a) 0% offset tension cone and (b) a 20% offset tension cone configuration.

B. Mass Estimation Results

The mass estimates for the three types of decelerators are shown below for the eight decelerator materials considered in this study. These mass results are for each decelerator type being attached to a 0.356 m diameter cylindrical bus. Figure 16 shows the mass estimates for the tension cone. Tension cones which use higher strength materials such as Vectran or Kevlar, exhibit significantly less overall mass, especially at larger diameters. Tension cones require an inflation system which increases the mass growth at an exponential rate due to its dependence on torus volume. Figure 17 shows the results for the attached isotensoid decelerator. Again, higher strength materials exhibit more mass efficient solutions. Figure 18 shows mass trends for the trailing isotensoid configuration which also follow almost linear mass growth rates. It is important to note that the mass calculations for the tension cone include estimates of inflation hardware, whereas the isotensoid calculations do not. The trailing isotensoid mass must be summed with a deployment system mass expected to be on the order of 1 kg, as shown in Figure 9. Attachment and storage mechanism are not included in any of these mass estimates.

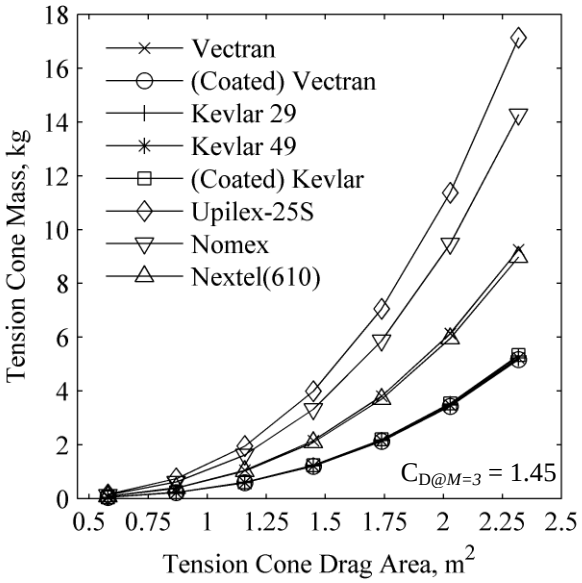

Figure 16. Decelerator mass as a function of drag area for a tension cone.

The estimated mass values are comparable to historical testing articles. The TD5840 test article consisted of a 1.5 m diameter attached isotensoid fabric mass was 1.9 kg deployed at a dynamic pressure of 5.75 kPa [69]. The TD 6929 attached isotensoid test article, also 1.5 m in diameter, had a mass of 0.98 kg tested up to dynamic pressures of 28 kPa [70].

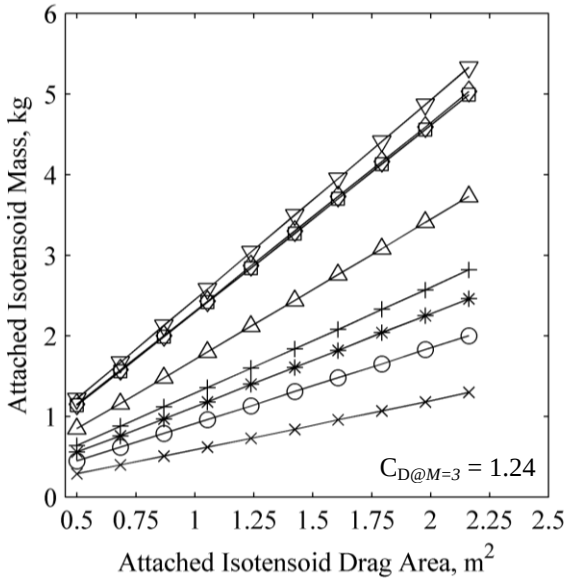

Figure 17. Decelerator mass as a function of drag area for an attached isotensoid

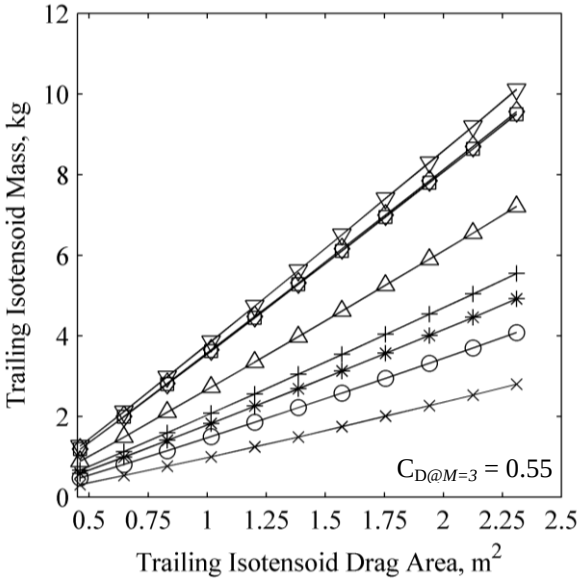

Figure 18. Decelerator mass as a function of drag area for a trailing isotensoid

C. Decelerator Evaluation

3. Vehicle Integration

Vehicle integration metrics were divided into four decelerator mechanisms: attachment, storage, deployment and inflation. These mechanisms encompass the primary functional modes of the decelerator systems and must be incorporated into interface considerations with the vehicle bus. Table VI below provides a brief description of each mechanism for each decelerator.

Table VI. Decelerator integration mechanisms and descriptions.

Mechanism	Tension Cone	Attached Isotensoid	Trailing Isotensoid
Attachment			
Location	Leading edge	Leading edge	Rear edge
Interface	Single *tension hoop*	2 *tension hoops* (one for front surface and one for rear surface)	1 or more *bridle attachment points*
Storage			
Location	Front (external to bus structure)	Front (external to bus structure)	Rear (internal or external to bus structure)
Devices	*Braided corset* used to wrap decelerator and fasten to bus	*Braided corset* used to wrap decelerator and fasten to bus	Packaged similar to that of a small parachute
Deployment			
Devices	*Pyrotechnic cutters* used to sever corset lacing and inflation system begins to release pressurized gas	*Pyrotechnic cutters* used to sever corset lacing and *pre-inflation gas generator* releases pressurized gas	*Mortar gun* ejects small mass to pull decelerator out and *pre-inflation gas generator* releases pressurized gas
Inflation			
Devices	*Internal inflation system* provides pressurized gas to decelerator	*Ram-air inlets* guide freestream air into the decelerator	*Ram-air inlets* guide freestream air into the decelerator

The devices italicized in Table VI are devices needed for their respective mechanisms. A description of each these devices and supplemental resources are found below:

- *Tension hoops* are devices that secure the fabric of the decelerator to the metal bus structure via a clamping mechanism. The fabric material is clamped between metal plates which are reinforced with bolts.
- *Bridle attachment points* are the location where the decelerator is fastened to the bus structure usually with bolts [36] [49].
- *Braided corset* is a tie-down device made of flexible material that is held together with lacing [71].
- *Pyrotechnic cutters* are devices that are capable of cutting cords using an explosive event [72].
- *Internal inflation system* is a gas generation system located within the vehicle bus. This device can be a pressure vessel with inert gas stored at high pressures or a system which expels gas as a by-product of a chemical reaction [73].
- *Pre-inflation gas system* is a gas generation system need to expose the ram-air inlets to the free stream. This is usually a small vial of methyl alcohol. The gas vaporized from this solution starts the inflation process for the isotensoid [61].
- *Mortar gun* is a small launcher that deploys a small lumped mass to being deployment process. [Sengupta]
- *Ram-air inlets* are devices that are located on the windward side of the decelerator and guide free stream air to the internal structure of the decelerator. [35] [69]

The priority weighting vectors for each integration mechanism from performing an AHP on each device and its associated metrics is shown in Table VII. These values were derived from discussions with the stake holders involved in this study.

Table VII. Vehicle integration mechanism weighted priority vectors.

Decelerator	Inflation Mechanism	Attachment Mechanism	Storage Mechanism	Deployment Mechanism	**Overall Weight Vector**
Tension Cone	0.026	0.017	0.047	0.091	**0.182**
Attached Isotensoid	0.106	0.015	0.047	0.091	**0.259**
Trailing Isotensoid	0.106	0.04	0.142	0.272	**0.559**

The isotensoid decelerator, from a vehicle integration perspective, has a less complex inflation mechanism since an onboard inflation system is not required. The attachment mechanism vector favored the trailing isotensoid in particular due to the extensive flight testing that has demonstrated the reliability of that mechanism. The attached isotensoid required multiple attachment points, which increases overall complexity of that system. Again, the storage and deployments mechanisms favor the heritage hardware of the trailing isotensoid.

The decelerator devices in a stowed configuration were examined using parachute packing densities. Without using pressurized packaging, the stowed decelerator packing density is estimated to be 320 kg/m^3 [49]. For the coated Vectran material, storage volume as a function of drag area for the three decelerator types is shown in Figure 19. The attached isotensoid is the most storage efficient while the trailing isotensoid requires the greatest storage volume. Storage volume could also be improved if pressurized packaging was implemented [74]. The priority vectors of both the design metrics and the vehicle integration mechanisms were combined into a TOPSIS analysis. Table VIII shows the relative closeness to the ideal for the three decelerators.

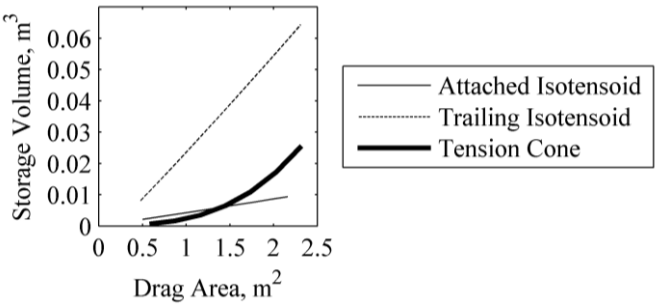

Figure 19. Decelerator storage volume as a function of decelerator drag area.

Table VIII. TOPSIS Euclidean distance to the ideal solution.

Decelerator Type	Relative Closeness to Ideal
Tension Cone	0.555
Attached Isotensoid	0.548
Trailing Isotensoid	0.448

The trailing isotensoid is calculated to be the more ideal configuration given the aforementioned input priority vectors. However, the tension cone and the attached isotensoid are found to be close to the trailing isotensoid. The tension cone exhibits the overall greatest aerodynamic performance but its required inflation system is detrimental to its vehicle integration score. The attached isotensoid exhibits the second best aerodynamic performance but its required two attachment points also increase its vehicle integration complexity. With proven flight test articles, the trailing isotensoid exhibits marginal aerodynamic performance and proven vehicle integration mechanisms.

VI. Architecture Results and Discussion

A. Dispersion Analysis Results

1. Trajectory Optimization

Single objective optimizations were performed using a gradient based algorithm using the following objective function formulation where λ is the launch elevation angle. Launch elevation angle was bounded between 77^0 - 85^0 specified by the NASA Sounding Rocket Handbook for the Improved-Orion sounding rocket [30].

Optimized trajectories for the cylindrical spacecraft configuration are shown in Figure 20. The trajectories are broken into specific phases. The sounding rocket provides thrust during the boost phase in a two segment (booster and sustainer) burn with final burnout occurring at 27 seconds after ignition. The payload and sounding rocket structure then enters a coast phase for approximately 10 seconds. The structural mass of the sounding rocket, approximately 110 kg, is then ejected and the vehicle bus enters a short duration despin phase (not modeled in this study) to prepare for sample collection. Sample collection occurs while the vehicle is above 45 km. The vehicle enters another coast phase once sample collection is complete. As the science objectives are independent of the deceleration technology, decelerators are not incorporated into these optimized trajectories, but are examined in following sections.

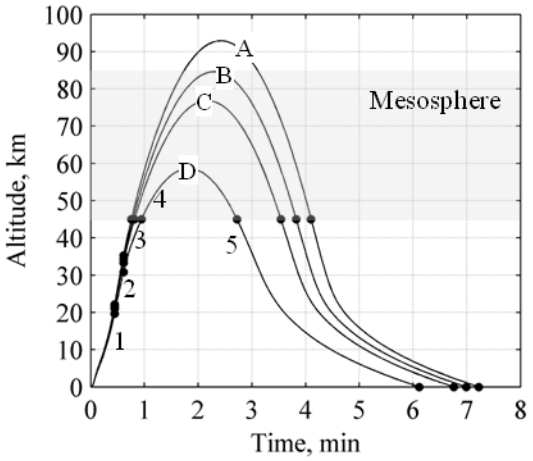

Phase	Description
1	Boost Phase
2	Coast Phase
3	Despin Phase
4	Sample Collection Phase
5	Descent & Recovery Phase

	Function Objective			
	Maximum number of 1 nm particles captured	Maximum time in the mesosphere	Maximum range in the mesosphere	Maximum collected sample mass
Trajectory	A	B	C	D
Launch Elevation Angle, Deg	82.5	80.9	79.9	77.0

Figure 20. Science objective optimized trajectory results.

The results indicate a sample collection efficient trajectory with a payload mass of 24 kg and launch elevation angle near 81 degrees is optimal. This trajectory provides the maximum time spent in the mesosphere, which translates to maximizing the likelihood of encountering mesospheric particles. This system configuration was established as the reference trajectory for the remainder of this study.

2. Drag Modulation Evaluation

Figure 21 shows downrange reduction performance for a sweep of trajectories with changes in launch elevation angle and vehicle bus mass. Maximizing time in the atmosphere requires a reasonably high launch angle (81°) which reduces overall drag modulation capability due to the more vertical nature of the trajectory. For a given launch elevation angle, lower mass payloads exhibited a degradation in drag modulated downrange performance. Lower mass payloads have a lower ballistic coefficient $\beta = m/(C_D A)$ for a given vehicle configuration which results in greater overall drag on the vehicle throughout its trajectory. For a nominal atmospheric and drag coefficient trajectory with deployment of a tension cone at 45 km altitude, a maximum of 10.25 km reduction is achieved for the lowest launch elevation angle relative to the no decelerator configuration. Following the boost phase, the earlier the decelerator is deployed during the trajectory, the more effective the drag modulation becomes. Approximately 10 km of downrange modulation capability is achievable when deployed at 50 km versus 25 km. It is assumed that the deployable can activate after apogee while still in the sample collection phase of flight. Sample collection is assumed to continue until 45 km altitude is reached during descent.

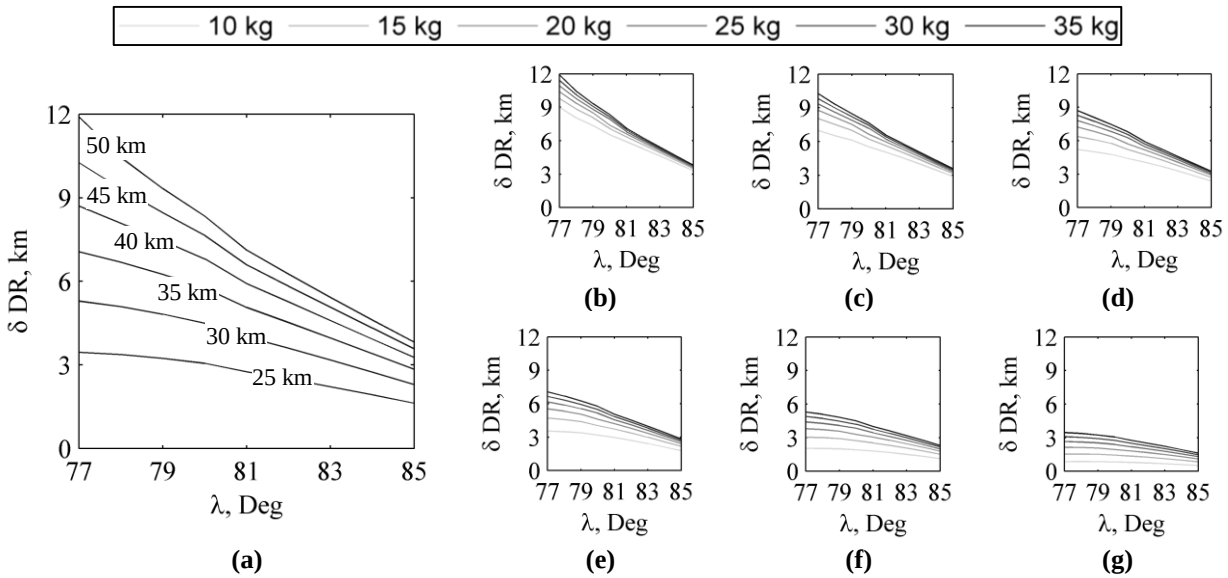

Figure 21. Downrange reduction using a 0.9 m diameter tension cone deployed at (a) altitudes between 25 and 50 km for a 35 kg mass payload; for payload masses ranging from 10 to 35 kg with deployment occurring at (b) 50 km , (c) 45 km, (d) 40 km, (e) 35km , (f) 30 km, (g) 25 km.

The deployment conditions of the IAD over the same sweep of system configurations are acceptable, as shown in Figure 22. The Mach number and dynamic pressures at deployment altitudes between 25 km and 50 km for a variety of payload masses and launch elevation angles all meet the deployment constraints of the IAD. The ballistic portion of the trajectory for a vehicle bus with a payload mass less than 20 kg becomes dominated by the aerodynamic drag, again due to its lower ballistic coefficient. As a result, less severe deployment environments over the range of deployment altitudes examined are experienced for lower mass systems. At the end of sample collection (45 km) the decelerator nominally would be deployed at Mach 3 and a dynamic pressure of 1 kPa.

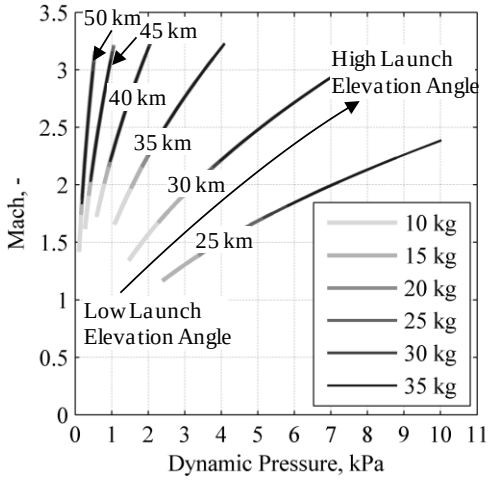

Figure 22. Mach vs. dynamic pressure at deployment altitudes of 25 to 50 km of a 0.9 m IAD as a function of launch elevation angle between 77^0 and 85^0 and payload masses between 10 and 35 kg.

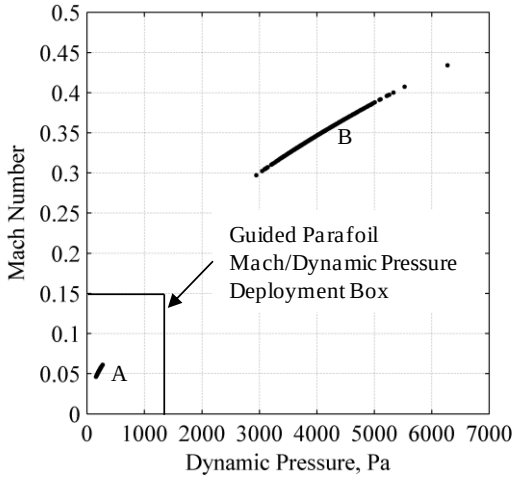

Figure 23. Mach vs. dynamic pressure parafoil deployment dispersions at 6 km altitude (A) with and (B) without IAD deployment at 45 km altitude.

Figure 23 shows the Mach and dynamic pressure conditions at the time of parafoil deployment (6 km altitude) for cases where an IAD is used (A) and is not used (B). Parafoil deployment when an IAD is deployed at 45 km achieves the required deployment constraints for this system. However, if no decelerator is deployed during in the trajectory, acceptable parafoil deployment conditions are not met.

Downrange reduction capability was also examined as a function of decelerator drag area, as shown in Figure 24. These trends were calculated using a launch elevation angle of 77^0 since this launch configuration provides the trajectory with the most horizontal flight path which maximizes the overall impact of drag modulation. As expected, the higher the IAD is deployed, the more effective the downrange reduction performance (upwards of 15 km for a 35 kg payload). However, as drag area is increased a diminishing return on downrange reduction is experienced due to trajectory effects. As the deployment altitude is reduced, increases the drag area of the decelerator is also shown to be less effective.

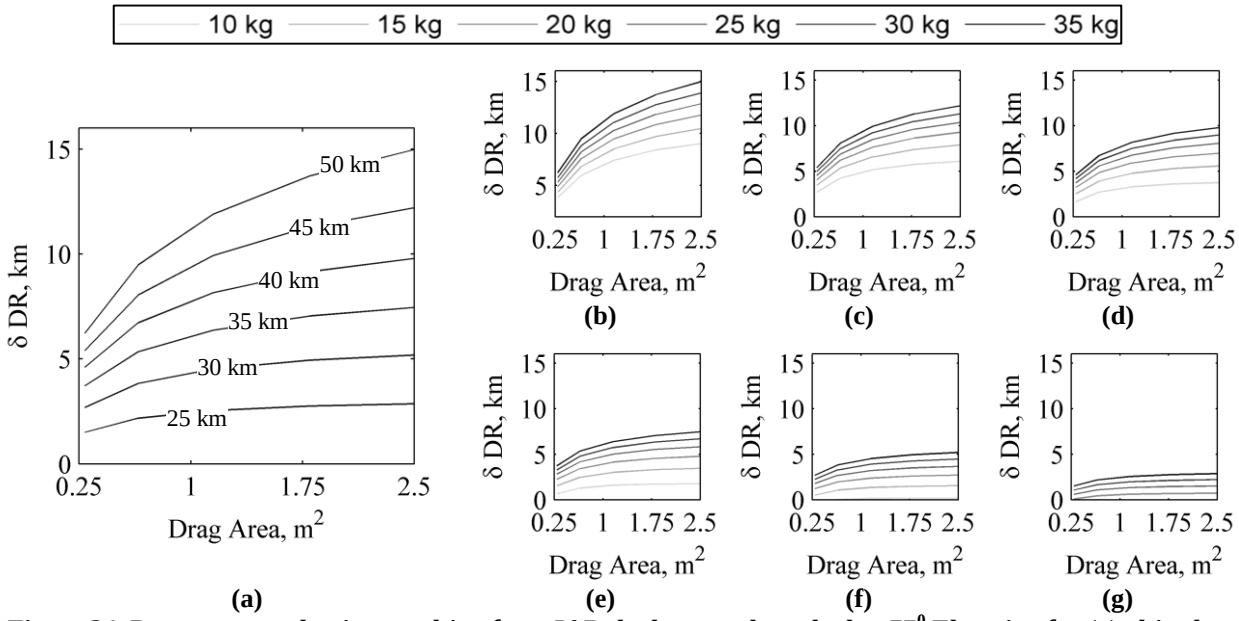

Figure 24. Downrange reduction resulting from IAD deployment launched at 77^0 Elevation for (a) altitudes between 25 and 50 km for a 35 kg mass payload; for payload masses ranging from 10 to 35 kg with deployment occurring at (b) 50 km , (c) 45 km, (d) 40 km, (e) 35km , (f) 30 km, (g) 25 km.

In order to assess the implementation of drag modulation, three 1000 run Monte Carlo simulations were conducted for (1) a DGB decelerator deployed at 73 km, (2) a 1.18 m^2 drag area IAD deployed at 45 km, and (3) a 1.18 m^2 drag area IAD deployed using the drag modulation algorithm (active between 25 and 45 km). Figure 25a shows the cumulative distribution functions (CDF) of the 2-norm range error for each system configuration. At the 95% confidence level, the DGB, IAD, and IAD with drag modulation produce range errors of 12.2 km, 11.6 km, and 9.7 km, respectively. This results in a 21% reduction in range error when IAD with drag modulation is implemented versus the stock option DGB decelerator. Implementation of drag modulation over a standard altitude deployment trigger of 45 km results shows a modest 16% reduction in range error. If the range capability of the parafoil is reduced to 5 km instead of 10km, drag modulation has a much more significant impact on the dispersion results. Approximately 76% of the disperse trajectories would land inside the reduced capability region, where as the DGB and IAD options would only achieve 55% and 61% success rates, respectively. Compared to the other decelerator options, the drag modulated IAD significantly improves the downrange precision capability of the system, as seen in Figure 25b. Table IX summarizes the statistics of the Monte Carlo analysis.

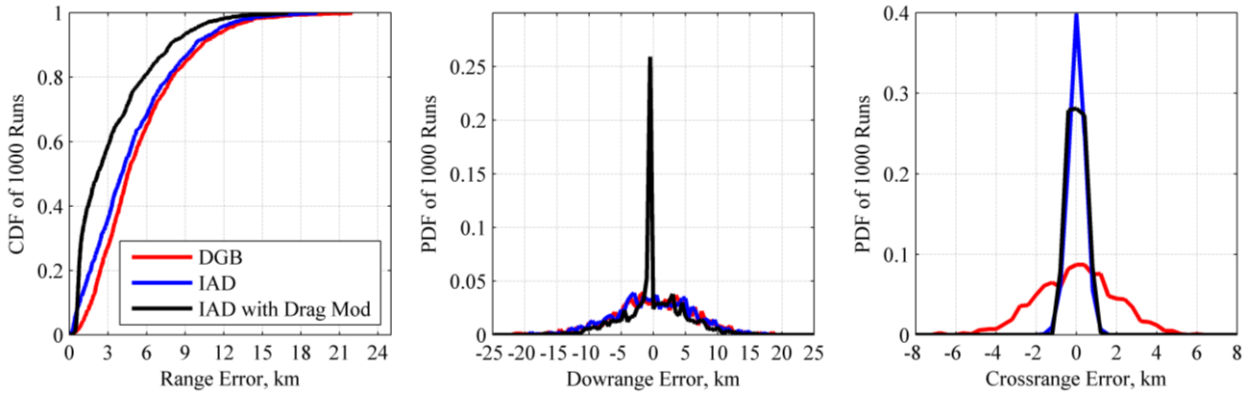

(a) **(b)** **(c)**

Figure 25. Range error for all three architectures. (a) CDF of the miss distance (b) PDF of the downrange error and (c) PDF of the crossrange error.

As shown in Figure 26, at the 95% confidence level, the DGB's downrange/crossrange footprint at 6 km altitude is 30.2 x 9.2 km. The IAD's downrange/cross range footprint is 29.1 x 1.2 km and with the addition of drag modulation, the IAD achieves a 22.2 x 2.0 km footprint. Although drag modulation reduced downrange dispersion, a slight increase in cross range dispersion is experienced. This is likely a result of the disparate altitudes of IAD deployment. If deployed early in the trajectory, the vehicle is more susceptible to lateral motion due to winds because of longer flight times. Two parafoil capability regions, a 10 km radius and a 5 km radius, represent various levels of performance of the guided parafoil. The larger radius region corresponds to a maximum capability region where as the smaller radius represents a less taxing option for parafoil system.

Table IX. Monte Carlo range error statistics.

Architecture	50% C.I. Range Error, km	75% C.I. Range Error, km	99% C.I. Range Error, km	Mean Error, km	Standard Deviation, km
DGB	4.53	7.31	16.70	5.40	3.52
IAD	4.10	6.78	15.21	4.79	3.53
IAD with Drag Mod	2.20	4.88	13.31	3.33	3.11

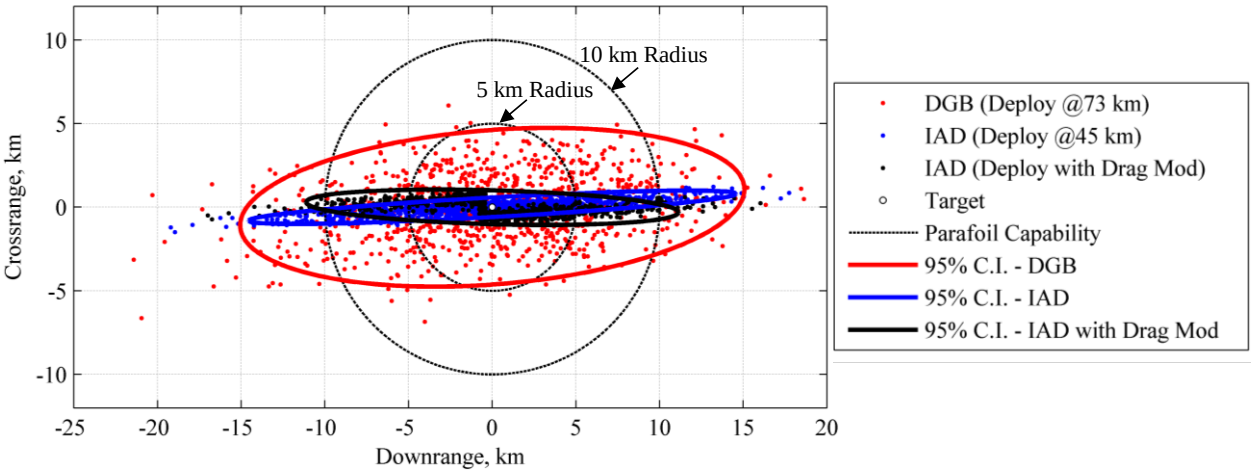

Figure 26. Downrange/Crossrange dispersions at 6 km altitude for DGB, IAD, and IAD with drag modulation with associated 95% confidence interval dispersion ellipses.

Cases that land within the capability regions, as shown in Figure 26, correspond to cases which have the ability to reach the target, thus reducing the landed dispersion to within one hundred meters. Inversely, cases that do not enter the capability region at an altitude of 6 km will not reach the desired target. Figure 27 below shows a

comparison of the cases that do not reach the capability regions for each decelerator system configuration as a percentage of the Monte Carlo cases that miss the capability regions. Drag modulation reduces the percentage of cases missing the 5 km capability region by 15%. When the capability region is expanded to 10 km, all three decelerator configurations exhibit significant improvement (<10% of the cases miss for all decelerator configurations). The use of an IAD, both deployed with a constant altitude trigger and a drag modulated trigger, marginally reduce the number of miss cases as compared to the DGB system by 2% and 5%, respectively. Overall, the 10 km capability region appears to be large enough to capture between 90%-95% of the Monte Carlo cases, regardless of the decelerator system implemented.

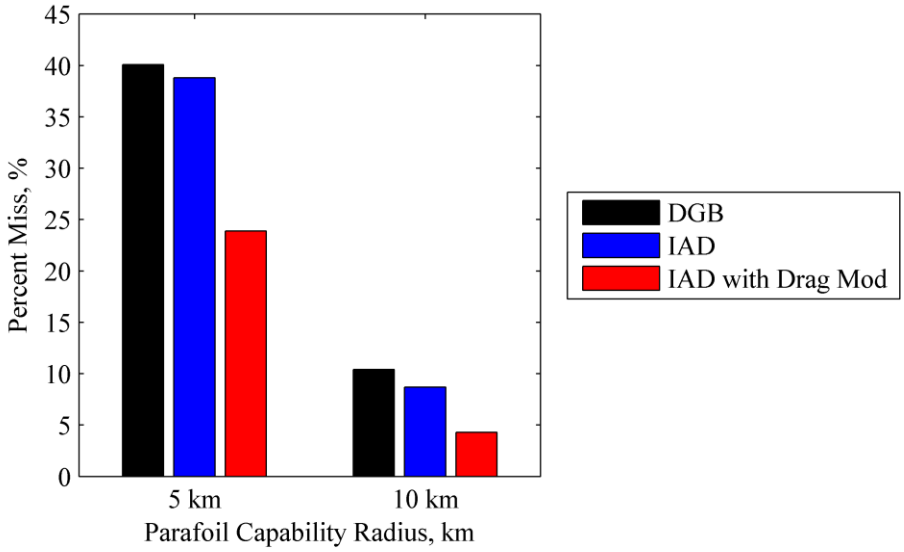

Figure 27. Monte Carlo cases which fail to reach the 5 km and 10 km parafoil capability radii for each decelerator configuration.

VII. Conclusion

The objective of this study was to evaluate three IAD configurations and the effect of IAD implemented drag modulation on a sounding rocket payload for atmospheric sample capture. A tension cone, attached isotensoid, and trailing isotensoid IAD were each investigated. Each IAD configuration was evaluated considering mass, aerodynamic performance, and vehicle integration. In terms of aerodynamic performance, the tension cone is the preferred choice for the sizes investigated. The attached isotensoid was shown to be the most mass efficient decelerator, while the trailing isotensoid was found to be the more ideal decelerator for vehicle integration. Heritage test vehicles have repeatedly proven the trailing isotensoid integration and deployment system. For the weighting considered, the trailing isotensoid was shown to be the preferred configuration for this mission.

Use of an IAD for downrange control was then demonstrated and deployment conditions were characterized for a variety of vehicle parameters. For the optimized reference trajectory, range error using drag modulation was shown to be reduced by 21% over existing DGB decelerators. Drag modulation control authority was shown to improve as payload mass increased and launch elevation angle decreased. Coupled with a precision guided parafoil, IAD drag modulation was shown to provide a 95% confidence level of success for landing with a 10 km parafoil capability region. The guided parafoil performance allows all (99%) of these cases to land within 100 m of the target. Use of an IAD, with or with drag modulation, was also found to ensure satisfactory deployment conditions of a guided parafoil. The examined architectures provide differing levels of engineering complexity, cost, and capability to be examined in future studies.

Acknowledgments

The work presented was funded by the C.S. Draper Laboratory, Inc. under a University Research and Development project entitled “Deployable Decelerators for Small Atmospheric Recovery Missions.” The authors would like to acknowledge Phil Hattis, Amer Fejzic, and Scott Thompson for their contributions to this investigation. The authors would also like to thank Christopher Cordell in the Space Systems Design Laboratory at Georgia Tech for contributions to the aerodynamics analysis presented in this work.

References

[1] S. Love and D. and Brownless, "A direct measurement of the terrestrial mass accretion rate of cosmic dust," *Science,* vol. 262, pp. 550-553, 1993.

[2] J. Mathews and e. al., "The micro-meteoroid mass flux into the upper atmosphere Arecibo results and a comparison with prior estimates," *Geophys. Res. Lett.,* vol. 28, pp. 1929-1932, 2001..

[3] R. Turco, O. Toon, R. Whitten, R. Keesee and D. Hollenbach, "Noctilucent clouds—simulation studies of their genesis, properties and global influences," *Planetary and Space Science,* vol. 30, p. 1147–1181, 1982.

[4] R. Goldberg, R. Pfaff, R. Holzworth and F. Smith, "DROPPS: A Study of the Polar Summer Mesosphere with Rocket, Radar and Lidar," *Geophysical Research Letters,* vol. 28.8, pp. 1407-1410, 2001.

[5] G. Stiller, "An enhanced HNO3 second maximum in the Antarctic midwinter upper stratosphere," *Journal of Geophysical Research,* vol. 110, 2003.

[6] M. Prather and J. Rodriguez, "Antarctic ozone: meteoric control of HNO3," *Geophysical research letters,* vol. 15, no. 1, 1988.

[7] D. Murphy, D. Thomson and M. Mahoney, "In Situ Measurements of Organizcs, Meteoritic Materials, Mercury, and Other Elements in Aerosols at 5 to 19 Kilometers," *Science,* vol. 282, 1998.

[8] R. Hawkes and S. Woodworth, "Do Some Meteorites Come from Interstellar Space?," *RASC Journal,* 1997.

[9] P. Soberman, "Extraterrestrial Dust Concentrations in the Upper Atmosphere," *Smithsonian Contributions to Astrophysics,* vol. 11, 1967.

[10] R. Saunders and J. Plane, "A laboratory study of meteor smoke analogues: composition, optical properties and growth kinetics," *J. Atmos. Sol.-Rerr. Phys.,* vol. 68, pp. 2182-2202, 2006.

[11] R. Soberman, C. Hemenway, T. Ryan, S. Chrest, J. Frissora and E. Fullham, "Micrometeorite Collection from a Recoverable Sounding Rocket I," *Smithsonian Contributions to Astrophysics,* vol. 7.

[12] M. Blanchard and N. Farlow, "Contamination control during the design, fabrication, test, and launch of an upper atmospheric rocket payload," *Contamination Control,* pp. 22-25, 1966.

[13] G. Ferry, M. Blanchard and N. Farlow, "Microparticle Collection Experiments during the 1966 Orionid and Leonid Meteor Showers," *Journal of Geophysical Research, Space Physics,* vol. 75, no. 4, 1970.

[14] R. Soberman and e. al., "Techniques for rocket sampling of noctilucent cloud particles," *Tellus,* 1964.

[15] N. Farlow, M. Blanchard and G. Ferry, "Sampling with a Luster Sounding Rocket during a Leonid Meteor Shower," *Journal of Geophysical Research, Space Physics,* vol. 71, 1966..

[16] A. McIntyre, "AFCRL Space Science Research During 1967 (Annual Report to COSPAR)," Air Force Cambridge Research Labs L G Hanscom Field Mass," Technical report AD-665 853 Special repts. no. 70, 1967.

[17] J. Hedin, J. Gumbel and M. Rapp, "The aerodynamics of smoke particle sampling," in *17th ESA Symposium on European Rocket and Balloon Programmes and Related Research*, Sandefjord, Norway, 2005.

[18] R. Goldberg and e. al., "The DROPPS program to study the polar summer mesosphere," *Greenhouse Gases, Aerosols and Dust,* vol. 28, pp. 1037-1046, 2001.

[19] T. Blix and E. Thrane, "Noctilucent clouds and regions with polar mesopheric summer echoes studied by means of rocket-borne electron and ion DC-probes," *Geophys. Res. Lett.,* vol. 20, p. 2303–2306, 1993..

[20] M. Rodríguez, *Analysis of the dynamical behavior of the Minidusty rocket payloads, and its influence on the plasma probe measurements,* Tromsø, Norway: MS Thesis. Department of Physics and Technology, University of Tromsø, 2007.

[21] B. Smiley, M. Rapp, T. A. Blix, S. Robertson, M. Horanyi, R. Latteck and J. Fiedler, "Charge and size distribution of mesospheric aerosol particles measured inside NLC and PMSE during MIDAS MaCWAVE," *J. Atmos. Sol. Terr. Phys.,* vol. 68, pp. 114-123, 2006.

[22] J. Gumbel and e. al., "The MAGIC campaign: An overview," in *17th ESA Symposium on European Rocket and Balloon Programmes and Related Research (ESA SP-590),* 2005.

[23] J. Hedin, J. Gumbel, T. Waldemarsson and F. Giovane, "The aerodynamics of the MAGIC meteoric smoke sampler," *Advances in Space Research,* vol. 40, pp. 818-824, 2007.

[24] J. Hedin, *Rocket-borne in-situ measurements in the middle atmosphere,* Stockholm, Sweden: PhD Thesis.

Department of Meteorology, Stockholm University, 2009.

[25] B. Smith, C. Tanner, M. Mahzari, I. Clark, R. Braun and F. Cheatwood, "A Historical Review of Inflatable Aerodynamic Decelerator Technology Development," in *2010 IEEE Aerospace Conference*, Big Sky, MT, 2010.

[26] F. Nebiker, "PEPP Ballute Design and Development Final Report," NASA – CR 66585, 1967.

[27] F. Nebiker, "Aerodynamic Deployable Decelerator Performance Evaluation Program, Phase I," AFFDL – TR67-27, 1965.

[28] I. Clark, M. Adler and T. P. Rivellini, "Development and Testing of a New Family of Supersonic Decelerators," in *AIAA Aerodynamic Decelerator Systems Conference*, Daytona Beach, FL, 2013.

[29] M. Miller, B. Steinfeldt and R. and Braun, "Mission Architecture Considerations for Recovery of High-Altitude Atmospheric Dust Samples," in *AIAA Atmospheric Flight Mechanics Conference*, Boston, MA, 2013.

[30] *NASA Sounding Rocket Handbook,* Goddard Spaceflight Center: Wallops Flight Facility, 2006.

[31] M. Burchell and e. al., "Characteristics of cometary dust tracks in Stardust Aerogel and laboratory calibrations," *Meteorite. Planet. Sci.,* vol. 43, pp. 23-40, 2008.

[32] D. e. a. Hunten, "Smoke and Dust Particles of Meteoric Origin in the Mesosphere and Stratosphere," *Journal of Atmospheric Sciences,* vol. 37, 1980.

[33] I. Clark, A. Hutchings, C. Tanner and R. and Braun, "Supersonic Inflatable Aerodynamic Decelerators for Use on Future Robotic Missions to Mars," *Journal of Spacecraft and Rockets,* vol. 46, no. 2, pp. 340-352, 2009..

[34] R. Barton, "Development of Attached Inflatable Decelerators for Supersonic Application," NASA CR-66613, 1968..

[35] C. Tanner, *Aeroelastic Analysis and Testing of Supersonic Inflatable Aerodynamic Decelerators,* Atlanta, GA: PhD Thesis. Department of Aerospace Engineering, Georgia Institute of Technology, 2012..

[36] J. Usry, "Performance of a Towed, 48-inch-Diameter Ballute Decelerator Tested in Free Flight at Mach Numbers from 4.2 to 0.4," NASA TN D-4943, Hampton, Va, 1969.

[37] G. Brown and R. Haggard, "Parafoil Mid-Air Retrieval For Space Sample," in *16th AIAA Aerodynamic Decelerator Systems Technology Conference and Seminar*, Boston, MA, 2001.

[38] A. Puranik, *Dynamics Modeling, Simulation and Control Design of a Parafoil-Payload System for Ship Launched Aerial Delivery Systems (SLADS),* PhD Thesis: Michigan Technological University, 2011.

[39] P. Hattis, D. Campbell, D. Carter and M. McConley, "Providing Means for Precision Airdrop Delivery from High," in *AIAA Guidance, Navigation, and Control Conference and Exhibit*, Keystone, Colorado, 2006.

[40] R. Benney, A. Meloni, M. Henry, K. Lafond, G. Cook, S. Patel and L. and Goodell, "Joint Medical Distance Support and Evaluation (JMDSE) Joint Capability Technology Demonstration (JCTD) & Joint Precision Air Delivery Systems (JPADS)," in *Special Operations Forces Industry Conference*, Tampa Bay, 2009.

[41] D. Kinney, "Aero-Thermodynamics for Conceptual Design," in *2004 AIAA Aerospace Sciences Meeting and Exhibit*, Reno, NV, 2004.

[42] "FUN3D Manual," NASA Langley, [Online]. Available: http://fun3d.larc.nasa.gov. [Accessed Oct 2009].

[43] W. Anderson and D. Bonhaus, "An Implicit Upwind Algorithm for Computing Turbulent Flows on Unstructured Grids," *Computers and Fluids*, vol. 23, pp. 1-22, 1994.

[44] J. P. Steinbrenner and J. Abelanet, "Anisotropic Tetrahedral Meshing Based on Surface Deformation Techniques," in *AIAA 45th Aerospace Sciences Meeting*, Reno, NV, 2007.

[45] R. McCoy, "MC Drag – A Computer Program for Estimating the Drag Coefficients of Projectiles," US ARMY ARRADCOM TRR ARBRL–TR–02293, 1981.

[46] M. B.R., D. Young and T. Okiishi, Fundamentals of Fluid Mechanics, Fourth Edition, New York: Wiley, 2002.

[47] M. Silbert, G. Gilbertson and A. Moltedo, "High Altitude Decelerator Systems," in *AIAA 10th Aerodynamic Decelerator Conference*, 1989.

[48] M. Silbert, "Deployment of a spin parachute in the altitude region of 260,000 ft," *Journal of Spacecraft and Rockets,* vol. 20, 1983.

[49] T. Knacke, Parachute Recovery Systems: Design Manual, Santa Barbara, CA, 1992.

[50] D. Toohey, *Development of a Small Parafoil Vehicle for Precision Delivery,* M.S. Thesis, M.I.T., 2005.

[51] Stara Technolgies Inc., [Online]. Available: http://www.miniairdrop.com/MOSQUITO.html. [Accessed June 2013].

[52] J. Samareh, "Estimating Mass of Inflatable Aerodynamic Decelerators Using Dimensionless Parameters," in *8th International Planetary Probe Workshop*, Portsmouth, Virginia, 2011.

[53] M. S. Anderson, H. L. Bohon and M. M. and Mikulus, "A Structural Merit Function for Aerodynamic Decelerators," NASA-TND-5535, 1969..

[54] J. Stein and C. Sandy, "Recent Developments in Inflatable Airbag Impact Attenuation Systems for Mars Exploration," in *AIAA Paper 2003-1900*, 2003.

[55] "Vetran Materials Datasheet," [Online]. Available: http://imattec.com/linked/vectran%20-%20technical%20data.pdf.

[56] "Kevlar Materials Datasheet," [Online]. Available: http://www2.dupont.com/Kevlar/en_US/assets/downloads/KEVLAR_Technical_Guide.pdf.

[57] R. Niccum, J. Munson and L. Rueter, "Investigation of Kevlar Fabric-Based Materials for Use with Inflatable Structures," NASA CR-2724, 1977.

[58] "Upilex Materials Datasheet," [Online]. Available: http://www.ube.com/content.php?pageid=81.

[59] "Nomex Materials Datasheet," [Online]. Available: http://www2.dupont.com/Personal_Protection/en_US/assets/downloads/nomex/Nomex_Technical_Guide.pdf.

[60] D. M. Wilson, "Statistical tensile strength of Nextel™ 610 and Nextel™ 720 fibers," 3M Metal Matrix Composites Department, St. Paul, Minnesota.

[61] F. Bloetscher, "Aerodynamic Deployable Decelerator Performance Evaluation Program, Phase II," AFFDL – TR67-25, 1967.

[62] L. Levy, "The Use of Drag Modulation to Limit the Rate at Which Deceleration Increases During Nonlifting Entry," NASA TN D-1037, Washington, DC, 1961.

[63] Z. Putnam and R. Braun, "Precision Landing at Mars Using Discrete-event Drag Modulation," in *23rd AAS/AIAA Spaceflight Mechanics Meeting*, Kauai, HI, 2013.

[64] C. Justus and F. Leslie, "The NASA MSFC Earth Glocbel Reference Atmospheric Model – 2007 Version," NASA TM-2008-215581, 2008.

[65] C. Karlgaard, R. Beck and A. Olds, "Ares I-X Trajectory Reconstruction: Methodology and Results," *Journal of Spacecraft and Rockets*, vol. 50, 2013.

[66] M. Smayda and C. Goyne, "Dispersion Reduction for a Sounding-Rocket Scramjet Flight Experiment," *Journal of Spacecraft and Rockets*, vol. 49, no. 3, pp. 522-528.

[67] T. Saaty, Multi criteria decision making: The analytic hierarchy process, New York: McGraw-Hill, 1980.

[68] J. Lafleur, "Probabilistic AHP and TOPSIS for Multi-Attribute Decision-Making under Uncertainty," in *2011 IEEE Aerospace Conference*, Big Sky, MT, 2011.

[69] H. Bohon and R. Miserentino, "Deployment and Performance Characteristics of 1.5m Attached Inflatable Decelerators from Mach 2.2 to 4.4," NASA TN D- 5840, NASA Langley Research Center, 1970.

[70] C. Willis and M. Mikulas, "Static Structural Tests of a 1.5-Meter-Diameter Fabric Attached Inflatable Decelerator," NASA Langley Research Center TN D-6929, Hampton, VA, 1972.

[71] D. Coatta and e. al., "Development and Testing of an 8 Meter Isotensoid Supersonic Inflatable Aerodynamic Decelerator," in *AIAA Aerodynamic Decelerator Systems (ADS) Conference*, Daytona Beach, Florida, 2013.

[72] Y. Chang, *Pyrotechnic Devices, Shock Levels And Their Applications*, Presented at Pyroshock Seminar, ICSV9, 2002.

[73] G. Brown, C. Epp, C. Graves, J. Lingard and M. Darly, *Hypercone Inflatable Supersonic Decelerator*, AIAA Paper 2003-2167, 2003..

[74] M. Ivanov and e. al., "“Entry, Descent and Landing Systems Analysis Study: Phase 2 Report on Mars Science Laboratory Improvement," NASA/TM-2011-216988, 2011.

[75] A. Brattli and e. al., "The ECOMA 2007 campaign: rocket observations and numerical modelling of aerosol particle charging and plasma depletion in a PMSE/NLC layer," *Ann. Geophys.*, vol. 27, 2009.